Research Square

Preprints are preliminary reports that have not undergone peer review.
They should not be considered conclusive, used to inform clinical practice,
or referenced by the media as validated information.

# Enhancing PLA Crystallinity and Thermal Stability through Esparto Microfiber Reinforcement: Implications for Sustainable 3D Printing

**Abderraouf GHERISSI**

a.gresi@ut.edu.sa

University of Tabuk

**Research Article**

**Keywords:** Esparto microfiber, PLA Biocomposite, Thermal properties, 3D printing

**Posted Date:** November 13th, 2026

**DOI:** https://doi.org/10.21203/rs.3.rs-11569724/v1

**License:** This work is licensed under a Creative Commons Attribution 4.0 International License.
Read Full License

**Additional Declarations:** No competing interests reported.

# Enhancing PLA Crystallinity and Thermal Stability through Esparto Microfiber Reinforcement: Implications for Sustainable 3D Printing

Abderraouf GHERISSI

Department of Mechanical Engineering, Faculty of Engineering, University of Tabuk, 47913 Tabuk, Saudi Arabia

a.gresi@ut.edu.sa

**Abstract**

Natural fiber reinforcement offers a route to control polymer crystallization and improve the processability of sustainable materials for additive manufacturing. This study introduces a processing-dependent assessment of PLA reinforced with 1 wt% Esparto microfibers, focusing on thermal stability, crystallization behavior, and potential for fused deposition modeling (FDM). Thermogravimetric analysis showed that the fibers remain thermally stable up to approximately 200°C, with major degradation occurring between 225 and 350°C. Esparto addition increased PLA crystallinity from 28.9% to 36.7%, reduced the cold-crystallization temperature from 121.82°C to 115.41°C, and raised the melting temperature from 159.81°C to 167.12°C, indicating enhanced heterogeneous nucleation. Melt spinning reduced composite crystallinity to 25.3%, demonstrating the influence of processing on polymer structure. Despite this reduction, the composite retained the crystallization benefits of Esparto reinforcement relative to spun PLA. These results establish a link between natural fiber-induced nucleation and processing-dependent thermal behavior, demonstrating the potential of low-content Esparto reinforcement for developing renewable PLA filaments. The findings provide a basis for optimizing processing conditions and advancing Esparto/PLA composites for sustainable FDM applications.

**Keywords:** Esparto microfiber; PLA Biocomposite; Thermal properties; 3D printing.

## 1. Introduction

Polylactic acid (PLA) is a bio-based thermoplastic widely used in additive manufacturing due to its renewable origin, biodegradability, mechanical properties, and processability. Its compatibility with fused deposition modeling (FDM) makes it suitable for filament-based 3D printing. However, its brittleness, low elongation at break, limited heat resistance, and slow crystallization restrict its applications [1–4]. Incorporating natural fibers and agricultural residues offers a sustainable approach

to improving stiffness, thermal properties, and crystallization behavior while reducing material costs [5–8].

Cellulose fibers have demonstrated potential for improving PLA properties. Tanpichai et al. [9] reported increases in Young's modulus, tensile strength, and modulus following the incorporation of cellulose microfibers and nanofibers. Similarly, Lezak et al. [10] showed that agricultural micropowders promote PLA crystallization and increase elastic modulus, although they may reduce ductility. Kovačević et al. [11] demonstrated the feasibility of producing PLA composites reinforced with Spanish broom fibers. Esparto grass (*Stipa tenacissima*), an abundant plant in North Africa traditionally used for paper production, represents another promising reinforcement. Maghchiche [5] developed Alfa fiber/PLA composites containing up to 40 wt% fibers and demonstrated their potential as sustainable materials.

Despite these developments, the effects of processing conditions on Esparto/PLA composites remain insufficiently understood, particularly during melt spinning [5,12,13]. This process combines elevated temperatures and shear stresses that may degrade cellulose fibers and induce PLA chain scission, affecting crystallinity, melting behavior, and thermal stability [14–17]. Understanding these effects is essential for optimizing composite processing and maintaining fiber integrity.

This study investigates Esparto microfiber-reinforced PLA through three objectives: (1) extracting and characterizing Esparto microfibers; (2) evaluating glass transition, cold crystallization, melting behavior, and crystallinity after extrusion compounding and melt spinning; and (3) assessing the influence of processing on the thermal stability of the fibers and polymer matrix [18–22]. Thermogravimetric analysis (TGA), differential scanning calorimetry (DSC), and morphological characterization are used to establish processing–structure–property relationships [23–27].

PLA-based biocomposites are also promising materials for FDM, which produces complex components through layer-by-layer deposition [28,29]. Natural fillers such as wood, bamboo, and cork can improve the properties and reduce the cost of PLA filaments [30,31]. However, successful printing requires adequate fiber dispersion, thermal stability, and fiber–matrix adhesion [32,33]. Given its thermal stability up to approximately 200°C and micron-scale dimensions, Esparto microfiber may be suitable for FDM filaments, although its applicability requires further investigation. This study therefore also examines the thermal behavior and processability of Esparto/PLA composites for potential 3D printing applications.

The remainder of the paper is organized as follows. Section 2 describes the materials, extraction procedures, composite preparation, and characterization methods. Section 3 presents and discusses the thermal properties of the extracted fibers, extruded composites, and melt-spun fibers. Section 4 summarizes the main findings and proposes strategies for optimizing processing conditions. Section 5 identifies future research directions.

## 2. Material and method

The raw Esparto stems, measuring between 80 and 100 cm in length, were harvested from the arid regions of North Africa (figure 1). The chemical composition of the Esparto plant used in this study is approximately 45% cellulose, 25% pentosan, 23% lignin, 5% wax, and 2% other components. Polylactic acid (PLA) was used as the polymer matrix. The PLA is a commercially available thermoplastic with a glass transition temperature (Tg) of approximately 60°C and a

melting temperature ranging between 150 and 180°C. PLA exhibits excellent resistance to oils and greases and can be easily processed by conventional melt-processing techniques.

Esparto microfibers were extracted from raw Esparto stems through a multi-step process combining mechanical decomposition and chemical treatments, followed by mechanical grinding.

The extraction protocol consists of five main steps as illustrated in Figure 2.a Each step progressively purifies the cellulose and reduces the fiber dimensions to the microfiber scale.

The five-step extraction process for Esparto microfibers are as follows:

Step 1: Mechanical Decomposition and Alkali Treatment

Raw Esparto fibers were treated with a 3N sodium hydroxide (NaOH) solution for 2 hours at 100°C. This step removes non-cellulosic components such as lignin, hemicellulose, and waxes from the fiber surface. The yield after this step was approximately 40% of the initial material.

Step 2: Chemical Softening

The extracted fibers from Step 1 underwent further treatment in a 5N NaOH solution for 24 hours at 100°C. This step further purifies the cellulose by breaking down remaining impurities and softening the fiber structure. The yield after this step was approximately 70% of the material from Step 1.

Step 3: Chemical Extraction of Microfibrils

The softened fibers were subjected to acid hydrolysis using sulfuric acid ($H_2SO_4$), followed by multiple purification steps including centrifugation, dialysis, and washing with distilled water until neutral pH was achieved. This step isolates cellulose microfibrils by breaking down larger fiber structures and removing amorphous regions. The yield after this step was approximately 65% of the material from Step 2.

Step 4: Extraction of micro-Cellulose fibers

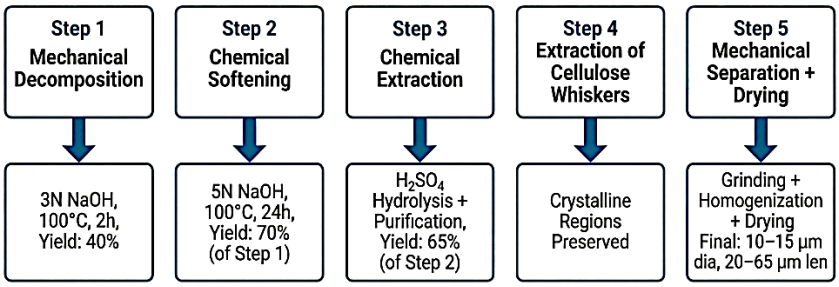
The hydrolyzed material was further treated to obtain individual elongated microcrystals, referred to as microfibers cellulose. Acid attack occurs preferentially in areas of disorganized microfibrils, leading to the individualization of crystalline parts. The resulting microfibers were collected and stored in aqueous suspension.

Step 5: Mechanical Separation and Drying

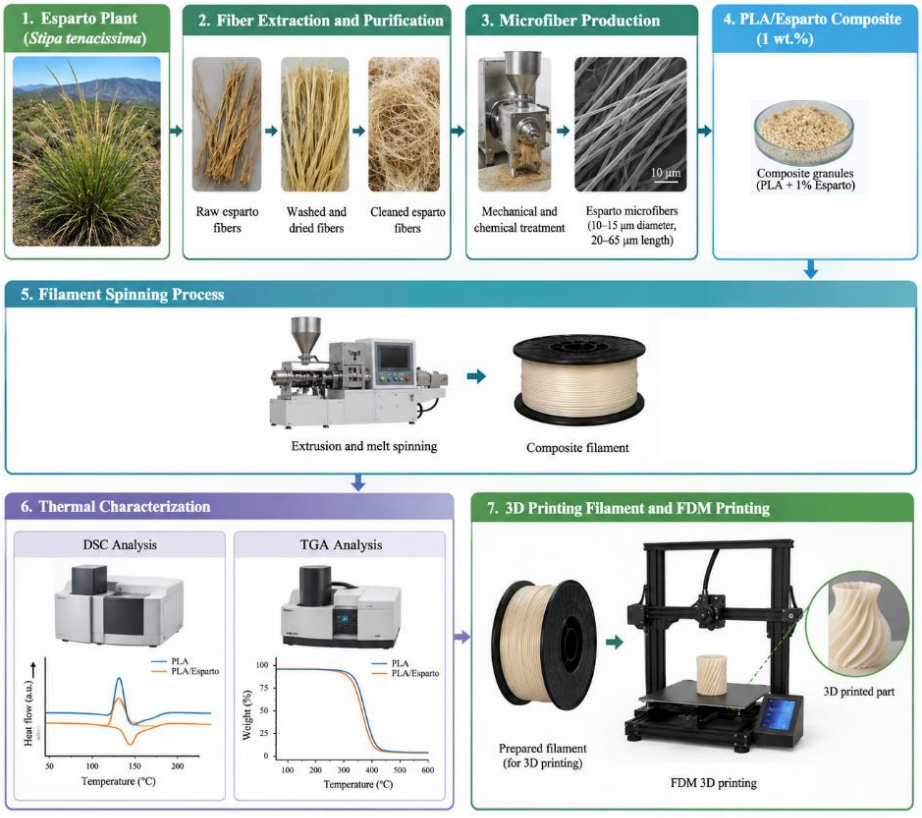
The final step involved mechanical grinding and high-shear homogenization to obtain finely separated Esparto microfibers. The obtained fibers were then dried and stored for composite preparation. The filaments were reduced to diameters ranging from 10 to 15 micrometers and lengths varying between 20 and 65 micrometers.



**Figure 1.** Esparto from the Natural Plant to micro-fibers




**(a)**




**(b)**

**Figure 2.** a-Schematic diagram of the five-step extraction process for Esparto microfibers

b-Process Flow Diagram: Esparto-PLA Composite Filament Preparation

The PLA/Esparto biocomposites were prepared by conventional extrusion compounding followed by melt spinning (Figure 2.b). The granules of PLA polymer and the extracted Esparto microfibers were mixed in a counter-rotating twin-screw extruder. The extrusion temperature profile was set between 150°C and 180°C, with a screw speed of 50 rpm. The extruded material was then cut into small granules suitable for the spinning process.

The composite fibers were spun using a spinning machine (Spinboy I, Busschaert Engineering). In this machine, the molten polymer is transported to a volumetric pump with a chamber volume of 7 $cm^3$. The rotational speed of the pump was set at 28 rpm, yielding a constant flow rate of 196 $cm^3$/min. The volumetric pump delivered the molten polymer through two channels, each consisting of 40 small channels of the same diameter (400 μm), producing two bundles of continuous monofilaments. These bundles were then condensed into a continuous multifilament, which was cooled by air circulation. The multifilament was coated with a sizing agent (Filapan CTC, a mixture of esters, acids, and branched polyglycols) to provide lubrication and cohesive inter-filament properties.

### 2.1. **Thermal Characterization via Differential Scanning Calorimetry (DSC)**

Differential scanning calorimetry analyses were performed using a DSC131 instrument equipped with a mechanical cooling system. The thermal transitions of both neat PLA and PLA/Esparto composites were analyzed at two processing stages:

(1) after extrusion compounding (granules) and (2) after melt spinning (fibers). Approximately 7 to 20 mg of each sample was sealed in aluminum crucibles (30 $mm^3$ volume) with pierced lids. An empty aluminum crucible was used as reference.

The analyses were conducted under a constant nitrogen flow (150 mL/min) using a two-cycle heating program. In the first cycle, samples were heated from 30°C to 230°C at a rate of 10°C/min to erase the thermal history, held isothermally for 5 minutes, and then cooled to 30°C at 10°C/min. The second heating cycle was performed under the same conditions to record the thermal transitions. The glass transition temperature (Tg), cold crystallization temperature (Tcr), melting temperature (Tf), and enthalpies of cold crystallization (ΔHcr) and melting (ΔHf) were determined from the second heating curves.

The degree of crystallinity of the PLA phase was calculated from the melting and cold crystallization enthalpies according to:

$$X_c(\%) = \frac{\Delta H_m - \Delta H_{cc}}{\Delta H_m^0 \, w_{\mathrm{PLA}}} \times 100 \qquad (1)$$

where $X_c$ is the crystallinity index (%), $\Delta H_m$ is the melting enthalpy (J/g), $\Delta H_{cc}$ is the cold crystallization enthalpy (J/g), $\Delta H_m^0$ is the theoretical melting enthalpy of 100% crystalline PLA, taken as 93 J/g [10,11], and $w_{\mathrm{PLA}}$ is the mass fraction of PLA in the sample.

For neat PLA: $w_{\mathrm{PLA}} = 1.00$

For the PLA/Esparto biocomposite containing 1 wt.% Esparto microfiber: $w_{\mathrm{PLA}} = 0.99$

When the cold crystallization peak is absent or its enthalpy is negligible, Equation (1) can be simplified to:

$$X_c(\%) = \frac{\Delta H_m}{\Delta H_m^0 \, w_{\mathrm{PLA}}} \times 100 \qquad (2)$$

The glass transition temperature, $T_g$, was determined from the midpoint of the glass transition region. It was calculated from the extrapolated onset and endset temperatures as:

$$T_g = \frac{T_{g,\mathrm{onset}} + T_{g,\mathrm{endset}}}{2} \qquad (3)$$

where $T_{g,\mathrm{onset}}$ is the onset temperature of the glass transition (°C), and $T_{g,\mathrm{endset}}$ is the endset temperature of the glass transition (°C).

The cold crystallization temperature, $T_{cc}$, was defined as the temperature corresponding to the maximum of the exothermic cold crystallization peak during the second heating cycle:

$$T_{cc} = T_{\mathrm{peak,exo}} \qquad (4)$$

where $T_{\mathrm{peak,exo}}$ is the temperature at the maximum of the cold crystallization exothermic peak (°C).

The melting temperature, $T_m$, was determined from the maximum of the endothermic melting peak during the second heating cycle:

$$T_m = T_{\mathrm{peak,endo}} \qquad (5)$$

where $T_{\mathrm{peak,endo}}$ is the temperature corresponding to the maximum of the melting endothermic peak (°C).

The change in heat capacity associated with the glass transition was determined from the difference between the heat capacities above and below $T_g$:

$$\Delta C_p = C_{p,\text{above}} - C_{p,\text{below}} \qquad (6)$$

where $\Delta C_p$ is the change in heat capacity, $C_{p,\text{above}}$ is the specific heat capacity above the glass transition, and $C_{p,\text{below}}$ is the specific heat capacity below the glass transition. The specific heat capacity is expressed in J/(g·K).

## 2.2. Thermal Characterization via Thermogravimetric Analysis (TGA)

Thermogravimetric analysis was performed using a TGA 2950 Thermogravimetric Analyzer (TGA 2950) instrument equipped with a Mac Bain electronic spring balance for high sensitivity. The thermal degradation behavior of neat PLA, Esparto microfibers, and PLA/Esparto composites at different processing stages was evaluated.

Approximately 10 mg of each sample was placed in a ceramic pan and heated from 100°C to 600°C at a heating rate of 10°C/min under a constant nitrogen flow of 40 mL/min. The weight loss and derivative weight loss (DTG) curves were recorded as a function of temperature.

The onset degradation temperature (Tonset), maximum degradation rate (Tmax), and residual mass at 600°C were determined for each sample. All TGA measurements were performed in triplicate, and the average results are reported.

The percentage mass loss at a given temperature was calculated as:

$$ML(\%) = \frac{m_i - m_T}{m_i} \times 100 \qquad (7)$$

where $ML$ is the mass loss (%), $m_i$ is the initial mass of the sample (mg), and $m_T$ is the sample mass at temperature $T$ (mg).

The residual mass at the end of the TGA analysis was calculated using:

$$RM(\%) = \frac{m_f}{m_i} \times 100 \qquad (8)$$

where $RM$ is the residual mass (%), $m_f$ is the final sample mass at the end of the TGA analysis (mg), and $m_i$ is the initial sample mass (mg).

For the present analysis, when the final temperature was 600 °C: $m_f = m_{600}$
The derivative thermogravimetric curve was obtained from the rate of change in sample mass with respect to temperature:

$$DTG = \frac{dm}{dT} \qquad (9)$$

Where $m$is the sample mass (mg) and $T$is the temperature (°C).

The DTG curve represents the rate of mass change as a function of temperature. The temperature corresponding to the maximum DTG peak was taken as the temperature of maximum degradation rate, $T_{\max}$.

The onset degradation temperature, $T_{\text{onset}}$, was determined using the tangent intersection method. A tangent was drawn along the initial stable region of the TGA curve and another tangent was drawn along the main descending region. The intersection of these two tangents was taken as the onset degradation temperature:

$$T_{\text{onset}} = T_{\text{intersection}} \qquad (10)$$

where $T_{\text{intersection}}$is the temperature corresponding to the intersection of the two tangents (°C).

The temperature of maximum degradation rate was determined from the maximum peak of the DTG curve:

$$T_{\max} = T_{\text{peak,DTG}} \qquad (11)$$

where $T_{\text{peak,DTG}}$is the temperature corresponding to the maximum DTG peak (°C).

The integral procedural decomposition temperature (IPDT) was calculated to provide an overall parameter describing the thermal stability of the material:

$$IPDT = A^* T_f \qquad (12)$$

where $IPDT$is the integral procedural decomposition temperature (°C), $A^*$is the area ratio, and $T_f$is the final temperature of the TGA analysis (°C).

The area ratio $A^*$was calculated as:

$$A^* = \frac{S_1 + S_2}{S_1 + S_2 + S_3} \qquad (13)$$

where $S_1$is the area associated with the initial stable region, $S_2$is the area associated with the main degradation region, and $S_3$is the area associated with the residual region of the TGA curve.

A higher IPDT value indicates greater thermal stability over the investigated temperature range.

The apparent activation energy of thermal degradation was determined using the Flynn–Wall–Ozawa (FWO) isoconversional method. The FWO equation can be expressed as:

$$\log_{10}(\beta) = \log_{10}\left(\frac{AE_a}{R\,g(\alpha)}\right) - 2.315 - 0.4567\frac{E_a}{RT} \qquad (14)$$

where $\beta$is the heating rate, $A$is the pre-exponential factor, $E_a$is the apparent activation energy, $R$is the universal gas constant, $T$is the absolute temperature (K), $g(\alpha)$is the integral conversion function, and $\alpha$is the degree of conversion. The universal gas constant is: $R = 8.314\ \text{J mol}^{-1}\ \text{K}^{-1}$

At a fixed conversion level $\alpha$, a linear relationship is obtained by plotting: $\log_{10}(\beta)$ versus $\frac{1}{T}$

The slope of this linear relationship is related to the activation energy according to:

$$E_a = -\frac{\text{slope}\times R}{0.4567} \qquad (15)$$

The degree of conversion, $\alpha$, was calculated from the change in sample mass during thermal degradation:

$$\alpha = \frac{m_i - m_T}{m_i - m_f} \qquad (16)$$

Where $\alpha$is the degree of conversion, $m_i$is the initial sample mass (mg), $m_T$is the sample mass at temperature $T$(mg), and $m_f$is the final sample mass at the end of the degradation process (mg).

The conversion varies between 0 and 1: $0 \leq \alpha \leq 1$. Where $\alpha = 0$ represents the initial state before degradation and $\alpha = 1$ represents the final state of the degradation process considered in the calculation.

## 3. Results

Figure 3 presents the thermogravimetric analysis (TGA) curve of the Esparto microfibres, showing the variation in sample weight as a function of temperature. The analysis was performed from room temperature to approximately 550 °C. The initial sample mass was 13.9850 mg.

The TGA curve shows several stages of mass loss. Up to approximately 100 °C, the sample exhibits a small weight reduction, with the remaining mass reaching 97.74%. This corresponds to a mass loss of about 2.26%, which can be attributed mainly to the evaporation of absorbed moisture and other low-temperature volatile components. The relatively small loss indicates that the Esparto microfibres contain a limited amount of physically absorbed water.

Between approximately 100 and 200 °C, the mass decreases gradually. At 206.67 °C, the remaining mass is 92.48%, corresponding to a cumulative mass loss of 7.52%. The decomposition becomes more pronounced above approximately 200 °C. At 225.21 °C, the remaining mass decreases to 89.24%. This temperature range can be associated with the beginning of the thermal degradation of the less stable constituents of the lignocellulosic structure, particularly hemicellulose and other low-molecular-weight components.

The main degradation region occurs approximately between 225 and 350 °C. The curve shows a rapid decrease in sample mass, indicating intensive decomposition of the organic constituents. This region is mainly related to the degradation of hemicellulose and cellulose, with cellulose contributing substantially to the major mass-loss stage. The degradation continues at a lower rate beyond 350 °C, which can be attributed to the progressive decomposition and carbonization of lignin and other thermally stable constituents.

Above approximately 450 °C, the mass decreases further and approaches zero near 500–520 °C. This indicates that most of the organic material has decomposed, leaving only a very small amount of thermally stable residue.

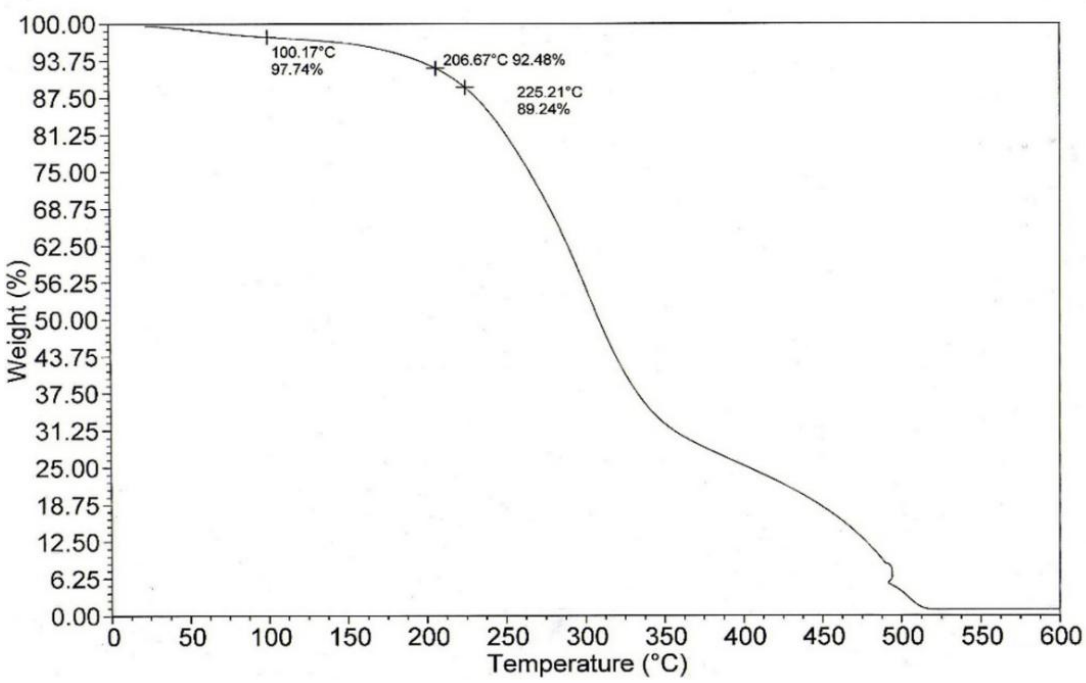



**Figure 3.** Curve TGA of microfibres of Esparto

The TGA results indicate that the Esparto microfibres exhibit thermal stability up to approximately 200 °C, since only a limited mass loss occurs below this temperature. The major

thermal degradation starts above approximately 200–225 °C, with the most significant weight reduction occurring between approximately 225 and 350 °C. Therefore, processing temperatures for Esparto-based composite materials should preferably remain below the onset of this major degradation region.

The initial degradation temperature of approximately 200–225 °C provides an important reference for selecting processing conditions. Temperatures substantially above this range may promote degradation of the natural fibres and consequently reduce their mechanical performance. The broad degradation region at higher temperatures also reflects the multicomponent nature of Esparto fibres, which contain cellulose, hemicellulose, lignin, and other minor constituents.

Overall, the TGA curve confirms the lignocellulosic nature of the Esparto microfibres and indicates that their useful thermal-processing range is limited by the onset of significant degradation above approximately 200 °C. The results support the use of relatively low-temperature composite manufacturing processes to preserve the fibre structure and avoid thermal damage.

Figure 4 presents the thermogravimetric analysis of pure PLA and PLA reinforced with 1% Esparto microfibres. The curves show the variation in mass as a function of temperature from 100 to 600 °C. Both materials exhibit similar thermal degradation behavior, with a small mass change at temperatures below approximately 250 °C, followed by a major mass-loss stage at higher temperatures.

The pure PLA remains relatively stable up to approximately 250 °C. The mass then decreases rapidly between approximately 270 and 340 °C, indicating the main thermal degradation of the PLA matrix. After this stage, only a small residue remains, which gradually decreases with increasing temperature and approaches zero at approximately 490–500 °C.

The PLA/Esparto composite shows a similar degradation pattern. However, its main mass-loss region is slightly shifted toward higher temperatures compared with pure PLA. The composite also maintains a higher mass during the main degradation stage. For example, around 300 °C, the PLA/Esparto composite retains a higher percentage of its initial mass than pure PLA. This indicates a small improvement in the thermal resistance of PLA after incorporating 1% Esparto microfibres.

The presence of Esparto microfibres introduces additional lignocellulosic components into the PLA matrix. These components undergo thermal degradation over a broader temperature range. At the same time, the interaction between the fibre and PLA matrix can influence the degradation process and delay the rapid decomposition of the polymer. Since the Esparto content is only 1%, the overall TGA profile remains dominated by the PLA matrix.

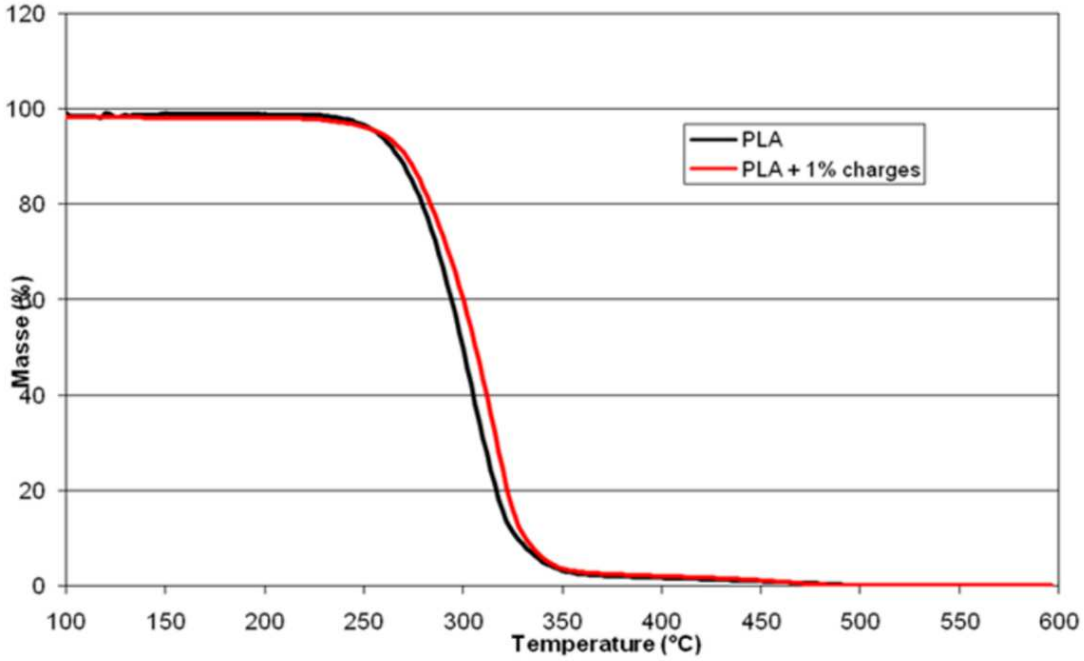



**Figure 4.** TGA of the pure PLA and PLA composite at 1% of Esparto microfibers

The TGA curves demonstrate that the addition of 1% Esparto microfibres does not significantly alter the overall thermal degradation behavior of PLA. However, the composite shows a slight shift of the main degradation region toward higher temperatures and a higher residual mass during the degradation stage.

The results suggest that incorporating a small amount of Esparto microfibres can improve the thermal stability of PLA to some extent. The relatively stable region below approximately 250 °C is important for processing the composite because it indicates that the material can be processed within this temperature range without causing the major degradation observed at higher temperatures. The comparison also shows that the main degradation of both materials occurs approximately between 270 and 340 °C. Therefore, the processing temperature should be selected below the onset of this major degradation region to limit thermal damage to both PLA and the Esparto fibres. This result supports the use of Esparto microfibres as a low-content natural reinforcement for PLA-based composite materials.

Figure 5 presents the differential scanning calorimetry (DSC) thermogram obtained during the second heating cycle of pure PLA granules prior to filament spinning. This analysis was performed to establish the baseline thermal behavior of the unmodified polymer matrix after extrusion compounding, serving as a reference for evaluating the effect of Esparto microfiber incorporation and the subsequent melt-spinning process. The DSC curve was recorded under a nitrogen atmosphere at a heating rate of 10°C/min, following an initial heating cycle to 230°C and controlled cooling to 30°C to erase the thermal history of the material.

The DSC results on figure 5, for pure PLA before spinning reveal several important features. The glass transition at 56.38°C is consistent with values reported in the literature for semicrystalline PLA, which typically range between 55°C and 60°C depending on molecular weight, stereochemistry, and thermal history [1,10]. The ΔCp value of -0.634 mW reflects the amount of amorphous material undergoing the transition.

The cold crystallization temperature of 121.82°C is relatively high, indicating that the PLA chains require significant thermal energy to achieve the mobility necessary for crystalline reorganization. This behavior is characteristic of PLA with low nucleation density, where the absence of heterogeneous nucleating agents delays the onset of crystallization during heating.

The melting temperature of 159.81°C falls within the expected range for PLA (150–180°C) and is consistent with the presence of α-crystals, which are the most common crystalline polymorph of PLA. The melting enthalpy of 26.84 J/g, when compared to the theoretical enthalpy of fusion for 100% crystalline PLA ($\Delta H_f^0$ = 93 J/g), yields a crystallinity index (Xc) of approximately 28.9%. This value represents the total crystallinity developed during both the cooling step and the cold crystallization process.

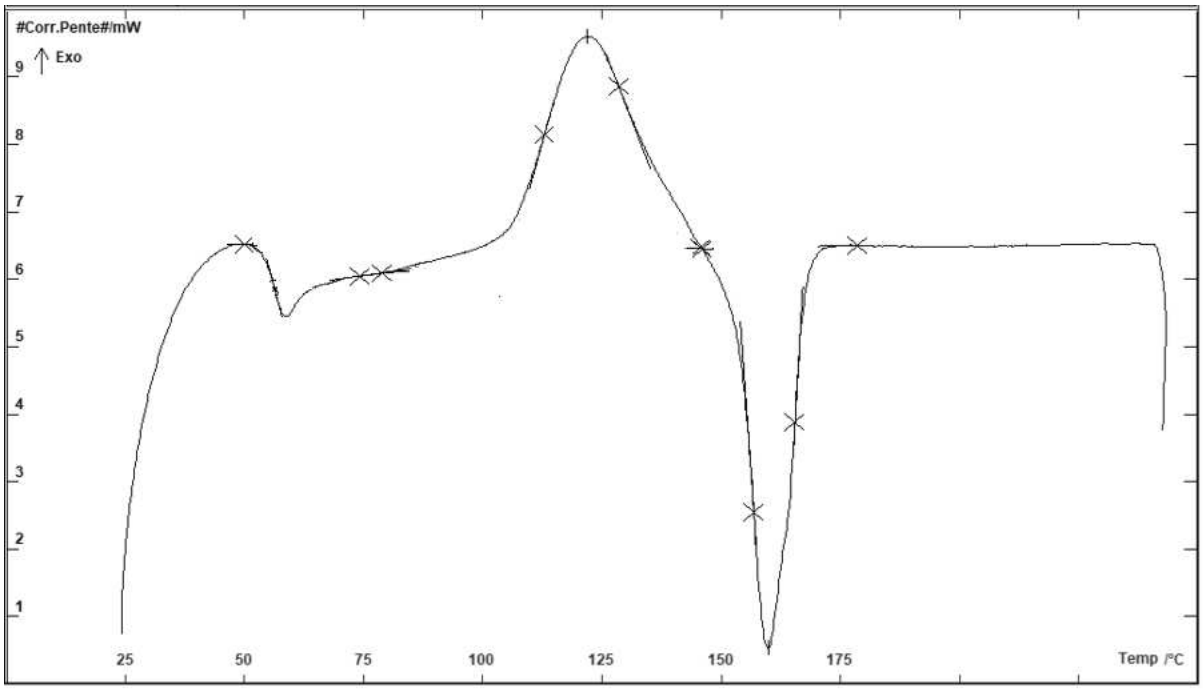



**Figure 5.** Differential Scanning Calorimetry (DSC) curves on pure PLA before filament spinning

Figure 6 presents the DSC thermogram obtained during the second heating cycle of PLA composite granules reinforced with 1% Esparto microfibers, prior to filament spinning. This analysis was performed to evaluate the effect of Esparto microfiber incorporation on the thermal transitions and crystallization behavior of the PLA matrix after extrusion compounding. The DSC curve was recorded under identical conditions to those used for pure PLA (Figure 5), namely a nitrogen atmosphere at a heating rate of 10°C/min, following an initial heating cycle to 230°C and controlled cooling to 30°C to erase the thermal history of the material. This allows for a direct and valid comparison between the neat polymer and the biocomposite.

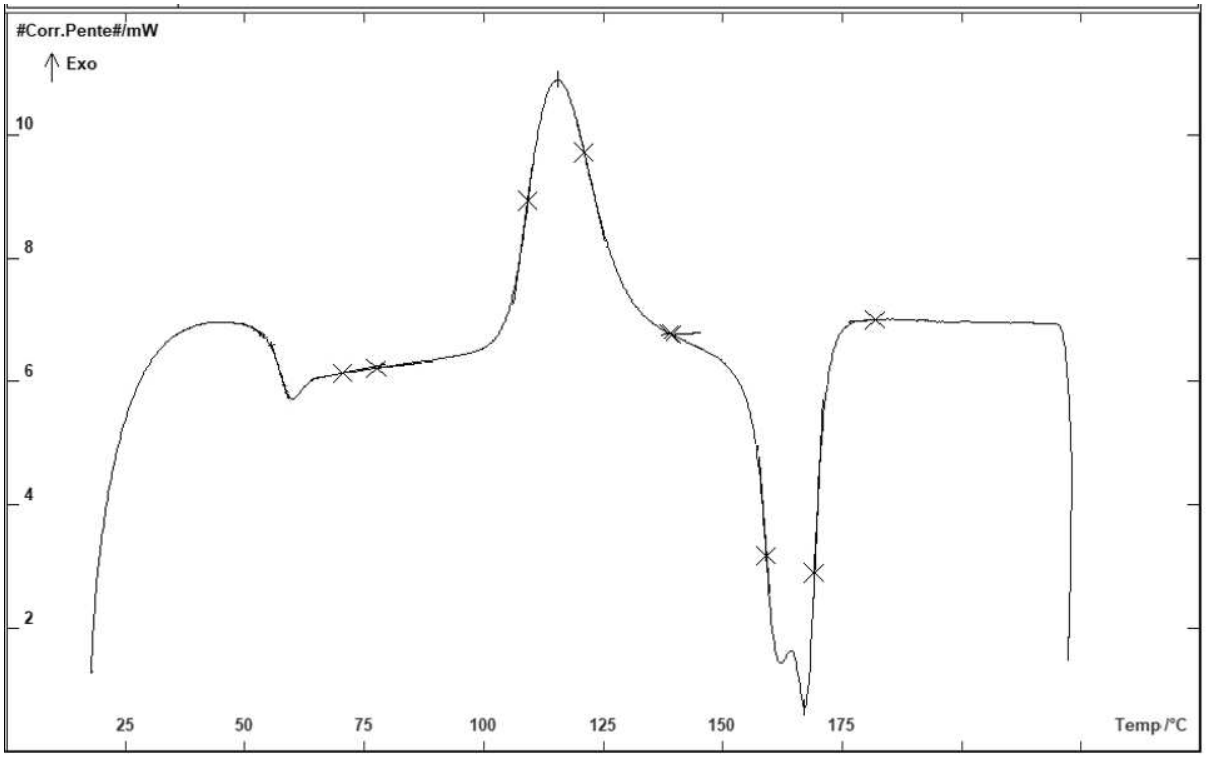



**Figure 6.** Differential Scanning Calorimetry (DSC) curves on composite PLA+1% of Esparto microfibers before filament spinning

The slight increase in Tg from 56.38°C (pure PLA) to 57.70°C (PLA + 1% Esparto) indicates a modest restriction of PLA chain mobility in the amorphous regions. This effect can be attributed to physical interactions between the PLA chains and the hydroxyl-rich surfaces of the Esparto microfibers, which create hydrogen bonding and dipole–dipole interactions that hinder segmental relaxation.

Similar increases in Tg have been reported for PLA composites reinforced with cellulose-based fillers. For instance, Kovačević et al. [11] observed an increase in Tg for PLA reinforced with Spanish broom fibers, attributing it to restricted chain mobility at the fiber–matrix interface. Ruz-Cruz et al. [14] also reported a slight increase in Tg for PLA/microfibrillated cellulose composites compared to neat PLA. However, the magnitude of the increase observed here (1.32°C) is relatively small, which is consistent with the low fiber loading (1%) and the absence of a coupling agent.

Figure 7 presents the DSC thermogram obtained during the second heating cycle of pure PLA fibers after melt spinning. This analysis was performed to evaluate the effect of the spinning

process on the thermal transitions and crystallization behavior of the PLA matrix. The DSC curve was recorded under identical conditions to those used for pure PLA before spinning (Figure 5), namely a nitrogen atmosphere at a heating rate of 10°C/min, following an initial heating cycle to 230°C and controlled cooling to 30°C to erase the thermal history of the material. This allows for a direct and valid comparison between the PLA granules before spinning and the PLA fibers after spinning, thereby isolating the effect of the spinning process on the thermal properties of the polymer.

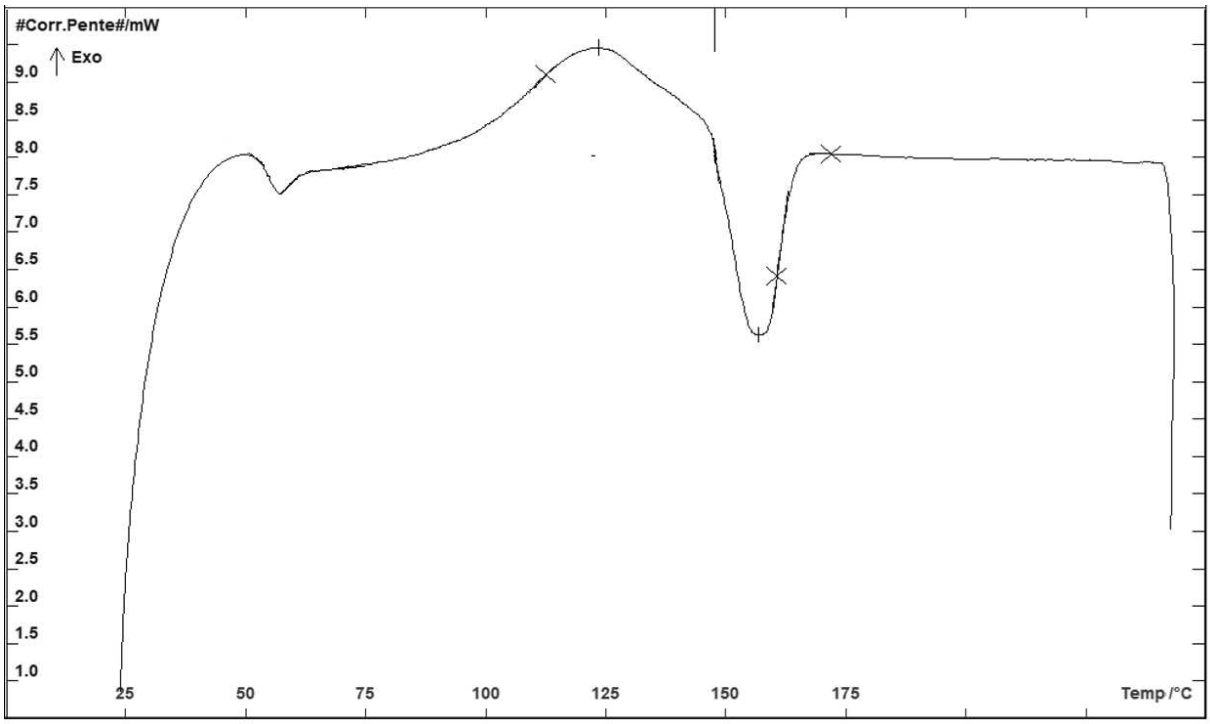



**Figure 7.** Differential Scanning Calorimetry (DSC) curves on pure PLA after filament spinning

The slight increase in Tg from 56.38°C (PLA granules before spinning) to 58.18°C (PLA fibers after spinning) indicates a restriction of PLA chain mobility in the amorphous regions after spinning. This effect can be attributed to the spinning process that induces molecular orientation along the fiber axis, which can restrict segmental mobility and increase Tg. The elongational flow during spinning aligns the polymer chains, reducing the free volume and increasing the energy required for segmental relaxation.

Figure 8 presents the DSC thermogram obtained during the second heating cycle of PLA composite fibers reinforced with 1% Esparto microfibers after melt spinning. This analysis was performed to evaluate the combined effects of Esparto microfiber incorporation and the

melt-spinning process on the thermal transitions and crystallization behavior of the PLA matrix. The DSC curve was recorded under identical conditions to those used for all previous samples (Figures 5–7), namely a nitrogen atmosphere at a heating rate of 10°C/min, following an initial heating cycle to 230°C and controlled cooling to 30°C to erase the thermal history of the material. This allows for a direct and valid comparison between the composite fibers and the other samples, thereby isolating the combined effects of fiber reinforcement and spinning on the thermal properties of the biocomposite.

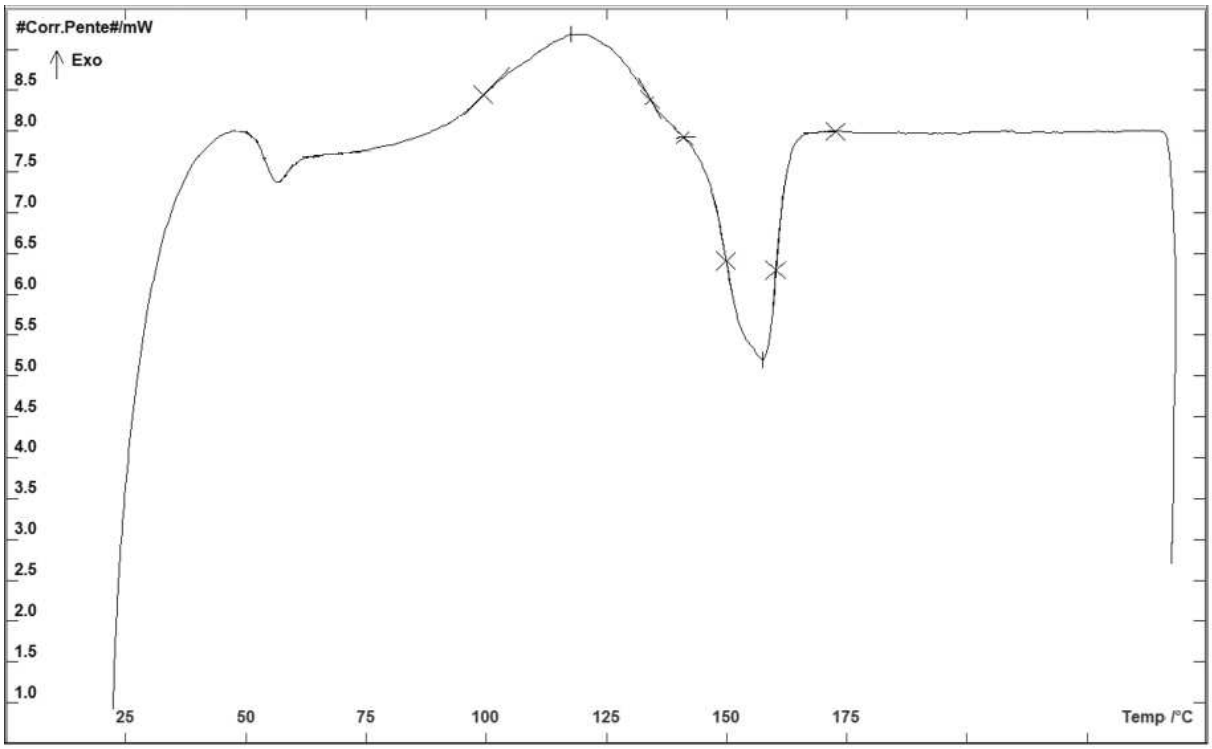



**Figure 8.** Differential Scanning Calorimetry (DSC) curves on composite PLA+1% of Esparto microfibers after filament spinning

The Tg of the PLA + 1% Esparto composite fiber after spinning (58.02°C) is slightly higher than that of the composite granules before spinning (57.70°C) and very close to that of the pure PLA fiber after spinning (58.18°C). This indicates that the spinning process is the primary factor responsible for the increase in Tg, rather than the presence of Esparto microfibers.

The increase in Tg after spinning can be attributed to molecular orientation along the fiber axis, which restricts segmental mobility and increases the energy required for relaxation. The elongational flow during spinning aligns the polymer chains, reducing free volume and

increasing Tg. Additionally, the rapid cooling of the fibers during spinning can trap residual stresses in the amorphous regions, further contributing to the increase in Tg.

The fact that the Tg values of the pure PLA fiber and the composite fiber after spinning are nearly identical (58.18°C vs. 58.02°C) suggests that the presence of 1% Esparto microfibers does not significantly affect the segmental mobility of the PLA chains in the amorphous regions after spinning. This is consistent with the low fiber loading and the dominant effect of the spinning process on the amorphous phase.

## 4. Discussion

### 4.1. The TGA and DSC results

The TGA and DSC analyses provide insight into the effects of 1% Esparto microfibers and melt spinning on the thermal stability and crystallization behavior of PLA. The results show that fiber incorporation promotes crystallization, whereas the spinning process modifies this effect through molecular orientation and thermal degradation.

The TGA curve of the extracted Esparto microfibers indicate that the Esparto microfibers remain stable up to approximately 200°C. Therefore, this temperature can be considered a practical upper processing limit for minimizing fiber degradation during melt processing.

The TGA curves of pure PLA and PLA containing 1% Esparto microfibers show a similar degradation pattern, with limited mass loss below 250°C followed by the main degradation stage between approximately 270 and 340°C. The composite exhibits a slight displacement of the main degradation region toward higher temperatures and a higher residual mass. This behavior suggests a modest improvement in the thermal resistance of PLA after fiber incorporation. The effect may be related to the presence of thermally stable lignocellulosic constituents and the formation of carbonaceous residues that can act as a diffusion barrier during thermal decomposition. Although the improvement is limited because of the low fiber content, the TGA results indicate that 1% Esparto does not adversely affect the thermal stability of the PLA matrix.

The DSC results provide further evidence of the influence of Esparto microfibers on PLA crystallization. Pure PLA granules before spinning exhibit a glass transition temperature (Tg) of 56.38°C, a cold crystallization temperature (Tcr) of 121.82°C, a melting temperature (Tf) of 159.81°C, and a crystallinity of 28.9%. After adding 1% Esparto microfibers, Tg increases

slightly to 57.70°C. This 1.32°C increase can be associated with restricted molecular mobility near the fiber–matrix interface.

More significant changes occur in the crystallization behavior. Tcr decreases from 121.82 to 115.41°C, corresponding to a reduction of 6.41°C, while crystallinity increases from 28.9% to 36.7%. The melting temperature also increases from 159.81 to 167.12°C, and the melting enthalpy reaches 34.16 J/g. These changes indicate that Esparto provides heterogeneous nucleation sites that facilitate PLA crystallization.

The increase in crystallinity of approximately 27% relative to the initial value demonstrates that the effect is significant even at a fiber loading of only 1%.

The effect of melt spinning becomes evident when the thermal properties of pure PLA before and after spinning are compared. Tg increases from 56.38 to 58.18°C, which can be related to molecular orientation and changes in chain mobility caused by the spinning process.

The cold crystallization temperature increases slightly from 121.82 to 123.39°C, while the crystallization onset decreases from 105.38 to 96.48°C. The lower onset temperature can be associated with orientation-induced nuclei formed during processing. In contrast, Tf decreases from 159.81 to 156.88°C, and the melting enthalpy decreases from 26.84 to 22.80 J/g. The crystallinity consequently decreases from 28.9% to 24.5%. These changes indicate that the thermal and shear conditions during spinning can promote PLA chain scission and modify the organization of the crystalline domains.

The effect is more pronounced for the PLA/Esparto composite after spinning, as shown in Figure 8. The composite fiber exhibits Tg = 58.02°C and Tcr = 117.60°C. Although Tcr increases relative to the unspun composite, it remains 5.79°C below that of the pure PLA fiber after spinning. This difference indicates that Esparto retains part of its nucleating function after melt spinning.

The cold crystallization onset occurs at 88.57°C, suggesting that oriented structures generated during spinning provide sites for early crystallization. However, the melting temperature decreases from 167.12°C before spinning to 157.47°C after spinning, while the melting enthalpy decreases to 23.51 J/g. Crystallinity also decreases substantially from 36.7% to 25.3%. The reduction is consistent with the combined effects of thermal exposure, shear, PLA chain scission, and possible degradation of the lignocellulosic phase during spinning.

The comparison between the two spun materials further confirms the residual nucleating effect of Esparto. Compared with pure PLA fibers, the PLA/Esparto fibers show a slightly lower Tg (58.02 versus 58.18°C), a lower Tcr (117.60 versus 123.39°C), a slightly higher Tf (157.47 versus 156.88°C), and slightly higher crystallinity (25.3% versus 24.5%). Thus, although

spinning reduces the crystallinity generated by fiber addition, the presence of Esparto still promotes crystallization relative to the spun PLA matrix.

The overall behavior can be explained by the competition between fiber-induced nucleation and processing-induced degradation. Before spinning, Esparto microfibers provide heterogeneous nucleation sites, reduce the energy barrier for PLA crystallization, and increase the crystalline fraction.

During spinning, molecular orientation can promote the formation of oriented nuclei, while elevated temperature, residence time, and shear can cause PLA chain scission and degradation of the cellulose-rich phase. The final thermal properties therefore reflect the balance between these two mechanisms. At 1% fiber loading, the nucleating effect remains measurable after spinning but is partly offset by the degradation associated with processing.

The obtained crystallinity of 36.7% for the unspun PLA/Esparto composite is comparable to values reported for PLA/microfibrillated cellulose systems containing substantially higher fiber contents. This observation supports the effectiveness of Esparto microfibers as nucleating agents. The 6.41°C reduction in Tcr is also consistent with the behavior reported for other cellulose-reinforced PLA systems. However, the reduction in crystallinity after spinning from 36.7% to 25.3% demonstrates that the processing conditions have a stronger influence on the final crystalline structure than fiber addition alone.

These findings have direct implications for melt-spinning process optimization. Processing temperatures should remain below the onset of significant Esparto degradation, particularly around 200–225°C. Residence time and shear should also be controlled to limit PLA chain scission and degradation of the fiber phase.

### 4.2. **3D Printing Potential and Advantages of Esparto Microfiber Addition**

The thermal behavior of the PLA/Esparto biocomposite indicates potential for application in fused deposition modeling (FDM) 3D printing. Thermal stability, crystallization behavior, and melt processing characteristics are key factors in the production and printing of thermoplastic filaments [28,29]. The TGA results show that Esparto microfibers remain relatively stable up to approximately 200°C, while the main degradation stage occurs between 225 and 350°C. This range is compatible with the processing conditions commonly used for PLA-based FDM, which generally operate at nozzle temperatures of approximately 190–220°C [30,31]. Therefore, at an appropriate processing temperature and residence time, substantial thermal degradation of the fibers during extrusion and printing can be limited.

The DSC results also indicate that Esparto addition modifies the crystallization behavior of PLA. The incorporation of only 1% Esparto increased the crystallinity from 28.9% to 36.7% and reduced the cold crystallization temperature from 121.82°C to 115.41°C. These changes indicate that the microfibers provide heterogeneous nucleation sites that facilitate PLA crystallization. For FDM applications, this behavior influence the development of the crystalline structure during cooling after layer deposition. Increased crystallinity can contribute to dimensional stability, stiffness, and thermal resistance, which are relevant properties for PLA components intended for engineering applications [32,33]. The lower cold crystallization temperature may also facilitate crystallization during the relatively short thermal cycle experienced by deposited layers [34,35].

The increase in melting temperature from 159.81°C for pure PLA to 167.12°C for the PLA/Esparto composite further indicates a modification of the crystalline structure following fiber incorporation. This shift may provide greater thermal stability of the solidified material during subsequent deposition cycles and could influence interlayer bonding and processing conditions [36,37].

The reduction in crystallinity observed after melt spinning, from 36.7% to 25.3%, highlights the importance of processing conditions. The spinning process used in this study involves thermal and shear conditions that differ from those encountered during conventional filament extrusion for FDM. Consequently, the reduction observed in the spun fibers cannot be directly transferred to FDM filaments. Optimized filament extrusion may involve different residence times, shear conditions, and thermal histories, which could reduce the extent of degradation and preserve a greater fraction of the nucleating effect of the Esparto fibers [38,39].

The relationship between melting behavior and interlayer adhesion depends on several additional parameters, including nozzle temperature, cooling rate, deposition speed, and substrate temperature. Therefore, experimental evaluation using actual FDM filament production is required to establish the extent to which the present thermal behavior translates into printing performance.

Esparto also offers a sustainability-related advantage. It is an abundant and underutilized natural resource in North Africa and can serve as a renewable fiber source for polymer composites. Its incorporation into PLA could reduce reliance on conventional synthetic fillers while supporting the development of bio-based materials for additive manufacturing [40,41]. In addition, the extracted Esparto microfibers have diameters of approximately 10–15 μm. Their micron-scale dimensions are suitable for investigation in filament extrusion because they are substantially shorter and finer than continuous or long-fiber reinforcement systems, which can present

greater risks of agglomeration and flow restrictions during extrusion and nozzle deposition [42,43].

Several processing challenges must nevertheless be addressed before Esparto/PLA filaments can be considered for practical FDM applications. Uniform fiber dispersion is required to prevent agglomeration and local variations in filament properties. The fiber concentration must also be optimized because increasing the reinforcement level may improve selected mechanical properties while affecting melt flow, filament diameter control, and nozzle flow. In addition, the hydrophilic nature of Esparto and the relatively hydrophobic character of PLA can limit interfacial adhesion. Fiber surface modification or the use of coupling agents may therefore be required to improve the fiber–matrix interface [44,45].

Future work should extend the present thermal investigation toward the fabrication of Esparto/PLA filaments specifically designed for FDM. Such studies should examine fiber loading, melt flow behavior, filament dimensional stability, extrusion temperature, nozzle temperature, printing speed, cooling conditions, and interlayer bonding. Mechanical characterization of printed specimens should include tensile, flexural, impact, and thermal performance, together with morphological analysis of the fiber distribution and fracture surfaces [46,47]. These experiments would establish whether the nucleating behavior and thermal stability observed in the present study can be translated into measurable improvements in the performance of FDM-printed Esparto/PLA components.

## 5. Conclusion

This study investigated the thermal stability and crystallization behavior of PLA reinforced with 1 wt% Esparto microfibers, considering the effects of extrusion compounding and subsequent melt spinning. The results demonstrate that Esparto microfibers can modify PLA crystallization while maintaining potential compatibility with filament-based additive manufacturing.

Thermogravimetric analysis showed that Esparto microfibers remain thermally stable up to approximately 200°C, with major degradation occurring between 225 and 350°C. Differential scanning calorimetry revealed that Esparto incorporation increased PLA crystallinity from 28.9% to 36.7%, reduced the cold-crystallization temperature from 121.82°C to 115.41°C, and increased the melting temperature from 159.81°C to 167.12°C. These changes confirm the nucleating effect of Esparto microfibers and their ability to modify the thermal transitions of the PLA matrix.

Melt spinning altered the thermal behavior of both pure PLA and the reinforced composite. The crystallinity of the Esparto/PLA composite decreased from 36.7% after extrusion to 25.3% after spinning, indicating that processing conditions influence the crystalline structure. Nevertheless, the persistence of the Esparto-induced crystallization effect highlights the potential of this natural reinforcement to retain its functional contribution after further melt processing. These findings emphasize the importance of controlling processing temperature, residence time, and shear conditions to balance fiber-induced nucleation with processing-related structural changes. The main contribution of this study is the evaluation of Esparto reinforcement across successive processing stages, providing insight into the relationship between fiber addition, crystallization behavior, and processing history. The results support the use of Esparto as a locally available, bio-based reinforcement for PLA filaments and provide a basis for further development of sustainable materials for fused deposition modeling (FDM). However, thermal characterization alone does not establish printability or improved mechanical performance, which require experimental validation.

Future research should investigate the effects of fiber loading and spinning conditions on thermal stability, crystallinity, and mechanical properties. The production and FDM printing of Esparto/PLA filaments should also be evaluated in terms of filament quality, nozzle flow, interlayer adhesion, dimensional stability, and printed-part performance. Finally, life cycle assessment and controlled end-of-life testing are needed to determine the environmental benefits and disposal characteristics of these composites.

**Funding**

This research received no external funding.

**Data Availability Statement**

The original contributions presented in this study are included in the article. Further inquiries can be directed at the corresponding author.

**Conflicts of Interest**

The author declares no conflicts of interest.

**Consent to Participate declaration:** not applicable

**Ethics declaration:** not applicable

## References


1. Ayyappan, V.; Rangappa, S. M.; Tengsuthiwat, J.; Fiore, V.; Siengchin, S. Investigation of Thermo-Mechanical and Viscoelastic Properties of 3D-Printed Morinda citrifolia Particle Reinforced Poly(lactic acid) Composites. Polymers 2024, 16, 1174. https://doi.org/10.3390/polym16081174
2. Aliotta, L.; Gigante, V.; Garofalo, G.; Baiamonte, M.; Molinari, G.; Lazzeri, A.; La Mantia, F. P.; Botta, L. Poly(lactic acid) (PLA)/Micro-Fibrillated Cellulose (MFC) Biocomposites for Film Blowing Applications. Polymers 2025, 17, 235. https://doi.org/10.3390/polym17020235
3. Wu, B.; Lu, W.; et al. Synergistic Enhancement of High-Barrier Polylactic Acid Packaging Materials by Various Morphological Carbonized Cellulose Nanocrystals. Carbohydrate Polymers 2025, 348, 122845. https://doi.org/10.1016/j.carbpol.2024.122845
4. Sabo, D.; Habibu, S.; Ladan, M.; Abdullahi, S.; Eric, D. Development of Starch-based Biodegradable Plastics Reinforced with Natural Fiber for Enhanced Mechanical and Biodegradation Properties. UMYU Scientifica 2025, 4(4), 338–358. https://doi.org/10.56919/usci.2544.030
5. Maghchiche, A. Characterisation of Esparto Grass Fibers Reinforced Biodegradable Polymer Composites. Biosciences Biotechnology Research Asia 2013, 10 (2), 665–673. https://doi.org/10.13005/bbra/1179
6. Zhao, X.; Liang, L.; Mo, F.; Dong, S.; Deng, C.; Liao, S.; Wu, H.; Zhou, L. Environment Friendly, Renewable and Sustainable Natural Fiber-Reinforced Polylactic Acid (PLA) Composites. Polymer Composites 2026, 47, S9. https://doi.org/10.1002/pc.70796
7. Tahir, M.; Seyam, A.-F. M. Greening Fused Deposition Modeling: A Critical Review of Plant Fiber-Reinforced PLA-Based 3D-Printed Biocomposites. Fibers 2025, *13*(5), 48. https://doi.org/10.3390/fib13050048
8. Gherissi, A., Cheikh, R. B., Dévaux, E., & Abbassi, F. (2011). Cellulose Whiskers Micro-Fibers Effect in the Mechanical Proprieties of PP and PLA Composites Fibers Obtained by Spinning Process. Applied Mechanics and Materials, 146, 12–26. https://doi.org/10.4028/www.scientific.net/amm.146.12
9. Tanpichai, S.; Wootthikanokkhan, J. Reinforcing Abilities of Microfibers and Nanofibrillated Cellulose in Poly(lactic acid) Composites. Science and Engineering of Composite Materials 2018, 25(2), 395–401. https://doi.org/10.1515/secm-2016-0145
10. Lezak, E.; Kulinski, Z.; Masirek, R.; Piorkowska, E.; Pracella, M.; Gadzinowska, K. Mechanical and Thermal Properties of Green Polylactide Composites with Natural Fillers. Macromolecular Bioscience 2008, 8(12), 1190–1200. https://doi.org/10.1002/mabi.200800040
11. Kovačević, Z.; Jurišić, V.; Grubor, M.; Matin, A.; Krička, T.; Bischof, S. Spanish Broom (Spartium junceum L.) – Feedstock for Bioplastic and Bioenergy Industry. Holistic Approach to Environment 2019, 9(3), 44–52. https://doi.org/10.33765/thate.9.3.1
12. Muthukumar, C.; Krishnasamy, S.; Thiagamani, S. M. K.; Ishak, M. R. B. (Eds.) Natural Fiber-Reinforced PLA Composites: Processing, Characterization and Applications; Woodhead Publishing: Cambridge, 2025. ISBN 978-0-323-95247-7. https://doi.org/10.1016/C2021-0-02728-0
13. Galera Manzano, L. M.; Ruz Cruz, M. A.; Moo Tun, N. M.; Valadez González, A.; Mina Hernandez, J. H. Effect of Cellulose and Cellulose Nanocrystal Contents on the Biodegradation, under Composting Conditions, of Hierarchical PLA Biocomposites. Polymers 2021, 13(11), 1855. https://doi.org/10.3390/polym13111855
14. Ruz-Cruz, M. A.; Herrera-Franco, P. J.; Flores-Johnson, E. A.; Moreno-Chulim, M. V.; Galera-Manzano, L. M.; Valadez-González, A. Thermal and Mechanical Properties of PLA-Based Multiscale Cellulosic Biocomposites. Journal of Materials Research and Technology 2022, 18, 485–495. https://doi.org/10.1016/j.jmrt.2022.02.072
15. Mazzanti, V.; de Luna, M. S.; Pariante, R.; Mollica, F.; Filippone, G. Natural Fiber-Induced Degradation in PLA-Hemp Biocomposites in the Molten State. Composites Part A 2020, *137*, 105990. https://doi.org/10.1016/j.compositesa.2020.105990
16. Jubinville, D.; Tzoganakis, C.; Mekonnen, T. H. Recycled PLA-Wood Flour Based Biocomposites: Effect of Wood Flour Surface Modification, PLA Recycling, and Maleation. Construction and Building Materials 2022, 352, 129026. https://doi.org/10.1016/j.conbuildmat.2022.129026
17. Zhan, J. H.; Wang, G. L.; Li, J.; et al. Effect of the Compatilizer and Chemical Treatments on the Performance of Poly(Lactic Acid)/Ramie Fiber Composites. Composites Communications 2021, 27, 100843. https://doi.org/10.1016/j.coco.2021.100843
18. Fortunati, E.; Armentano, I.; Iannoni, A.; Kenny, J. M. Development and Thermal Behaviour of Ternary PLA Matrix Composites. Polymer Degradation and Stability 2010, 95, 2200–2206. https://doi.org/10.1016/j.polymdegradstab.2010.03.001

19. Nekkaa, S.; Guessoum, M.; Haddaoui, N. Water Absorption Behavior and Impact Properties of Spartium junceum Fiber Composites. International Journal of Polymeric Materials 2009, 58, 468–481. https://doi.org/10.1080/00914030902936618
20. Nekkaa, S. , F. Chebira and N. Haddaoui . Effect of Fiber Treatment on The Mechanical and Rheological Properties of Polypropylene/Broom Fiber Spartium Junceum Composites. https://doi.org/10.36478/jeasci.2006.278.283
21. Govorčin Bajsić, E.; Meheš, M.; Kratofil Krehula, L.; Filipan, V.; Sutlović, I. Preparation and Thermal Properties of Thermoplastic Composites Filled with Spartium junceum L. Fibres. NANOCON Conference Proceedings 2024. https://doi.org/10.37904/nanocon.2023.4812
22. Zahedi, M.; et al. Development of a Novel Sandwich-Structured Composite from Biopolymers and Cellulose Microfibers for Building Envelope Applications. Scientific Reports 2023, 13, 22005. https://doi.org/10.1038/s41598-023-49273-0
23. Mohammed, L.; Ansari, M. N. M.; Pua, G.; Jawaid, M.; Islam, M. S. A Review on Natural Fiber Reinforced Polymer Composite and Its Applications. International Journal of Polymer Science 2015, 2015, 243947. https://doi.org/10.1155/2015/243947
24. Wafa Ouarhim, Nadia Zari, Rachid Bouhfid, Abou el kacem Qaiss, 3 - Mechanical performance of natural fibers–based thermosetting composites, Editor(s): Mohammad Jawaid, Mohamed Thariq, Naheed Saba, In Woodhead Publishing Series in Composites Science and Engineering, Mechanical and Physical Testing of Biocomposites, Fibre-Reinforced Composites and Hybrid Composites, Woodhead Publishing, 2019, Pages 43-60, ISBN 9780081022924, https://doi.org/10.1016/B978-0-08-102292-4.00003-5.
25. Feng, L. N.; Yahya, M. Y.; et al. Performance of the PLA-Based Biocomposites and Bionanocomposites under Dynamic Loads. In Natural Fiber-Reinforced PLA Composites; Woodhead Publishing, 2025; Chapter 4.
26. Parthasarathy, V.; Dinesh Babu, M.; et al. Advanced PLA Biocomposites for Tissue Engineering and Drug Delivery Applications. In Natural Fiber-Reinforced PLA Composites; Woodhead Publishing, 2025; Chapter 12, pp 309–318.
27. Yang, Z.; Sun, K. Enhanced Characterization of Wheat Straw-PLA Composites with Silane Coupling Agent and Alkali Pretreatment. Ecotoxicology and Environmental Safety 2025, 290, 117612. https://doi.org/10.1016/j.ecoenv.2024.117612
28. Bhayana, M.; Singh, J.; Sharma, A.; Gupta, M. A Review on Optimized FDM 3D Printed Wood/PLA Bio Composite Material Characteristics. *Materials Today: Proceedings* 2023, 78, 1–7. https://doi.org/10.1016/j.matpr.2023.03.029
29. Ayrilmis, N. Effect of Layer Thickness on Surface Properties of 3D Printed Materials Produced from Wood Flour/PLA Filament. *Polymer Testing* 2018, 71, 163–169. https://doi.org/10.1016/j.polymertesting.2018.09.009
30. Kariz, M.; Sernek, M.; Obućina, M.; Kuzman, M. K. Effect of Wood Content in FDM Filament on Properties of 3D Printed Parts. *Materials Today Communications* 2018, ,14, 135–140. https://doi.org/10.1016/j.mtcomm.2017.12.016
31. Tao, Y.; Wang, H.; Li, Z.; Li, P.; Shi, S. Q. Development and Application of Wood Flour-Filled Polylactic Acid Composite Filament for 3D Printing. *Materials* 2017, ,10,(4), 339. https://doi.org/10.3390/ma10040339
32. Le Guen, M. J.; Hill, S.; Smith, D.; Theobald, B.; Gaugler, E.; Barakat, A.; Mayer-Laigle, C. Influence of Rice Husk and Wood Biomass Properties on the Manufacture of Filaments for Fused Deposition Modeling. *Frontiers in Chemistry* 2019, 7, 478. https://doi.org/10.3389/fchem.2019.00478
33. Bhagia, S.; Lowden, R. R.; Erdman, D.; Rodriguez, M.; Haga, B. A.; Solano, I. R. M.; Gallego, N. C.; et al. Tensile Properties of 3D-Printed Wood-Filled PLA Materials Using Poplar Trees. *Applied Materials Today* 2020, 21, 100832. https://doi.org/10.1016/j.apmt.2020.100832
34. Zhao, X.; Tekinalp, H.; Meng, X.; Ker, D.; Benson, B.; Pu, Y.; Ragauskas, A. J.; et al. Poplar as Biofiber Reinforcement in Composites for Large-Scale 3D Printing. *ACS Applied Bio Materials* 2019, 2,(10), 4557–4570. https://doi.org/10.1021/acsabm.9b00675
35. Zarna, C.; Ching-Carrasco, G.; Echtermeyer, A. T. Bending Properties and Numerical Modelling of Cellular Panels Manufactured from Wood Fibre/PLA Biocomposite by 3D Printing. *Composites Part A: Applied Science and Manufacturing* 2023, 165, 107368. https://doi.org/10.1016/j.compositesa.2022.107368
36. Awad, S.; Siaken, R.; Khalaf, E. M.; Mahmoud, M. H.; Fouad, H.; Jawaid, M.; Sain, M. Evaluation of Characterisation Efficiency of Natural Fibre-Reinforced Polylactic Acid Biocomposites for 3D Printing Applications. *Sustainable Materials and Technologies* 2023, 36, e00620. https://doi.org/10.1016/j.susmat.2023.e00620

37. Das, A. K.; Agar, D. A.; Rudolfsson, M.; Larsson, S. H. A Review on Wood Powders in 3D Printing: Processes, Properties and Potential Applications. *Journal of Materials Research and Technology* 2021, 15, 241–255. https://doi.org/10.1016/j.jmrt.2021.07.110
38. Rajendran Royan, N. R.; Leong, J. S.; Chan, W. N.; Tan, J. R.; Shamsuddin, Z. S. B. Current State and Challenges of Natural Fibre-Reinforced Polymer Composites as Feeder in FDM-Based 3D Printing. *Polymers* 2021, 13, (14), 2289. https://doi.org/10.3390/polym13142289
39. Ramaux, J.; Ziegler-Devin, I.; Besserer, A.; Nouvel, C. 3D Printing of Wood Composites: State of the Art and Opportunities. *Polymers* 2024, 16 (19), 2827. https://doi.org/10.3390/polym16192827
40. Al Rashid, A.; Khan, S. A.; Koç, M. Life Cycle Assessment on Fabrication and Characterization Techniques for Additively Manufactured Polymers and Polymer Composites. *Cleaner Environmental Systems* 2024, 12, 100159. https://doi.org/10.1016/j.clesys.2023.100159
41. Ulkir, O. Energy-Consumption-Based Life Cycle Assessment of Additive-Manufactured Product with Different Types of Materials. *Polymers* 2023, 15 (6), 1466. https://doi.org/10.3390/polym15061466
42. Mazur, K. E.; Borucka, A.; Kaczor, P.; Gadek, S.; Bogucki, R.; Mirzewinski, D.; Kuciel, S. Mechanical, Thermal and Microstructural Characteristic of 3D Printed Polylactide Composites with Natural Fibers: Wood, Bamboo and Cork. *Journal of Polymers and the Environment* 2022, 30, 2341–2354. https://doi.org/10.1007/s10924-021-02356-3
43. Fabijanski, M. Properties of Composites Based on Polylactide Filled with Cork Filler. *Journal of Composites Science* 2024, 8, 185. https://doi.org/10.3390/jcs8050185
44. Xie, Y.; Hill, C. A. S.; Xiao, Z.; Militz, H.; Mai, C. Silane Coupling Agents Used for Natural Fiber/Polymer Composites: A Review. *Composites Part A: Applied Science and Manufacturing* 2010, 41(7), 806–819. https://doi.org/10.1016/j.compositesa.2010.03.005
45. Kovačević, Z.; Bischof, S.; Fan, M. The Influence of *Spartium junceum* L. Fibers Modified with Montmorillonite Nanoclay on the Thermal Properties of PLA Biocomposites. *Composites Part B: Engineering* 2015, 101, 122–130. https://doi.org/10.1016/j.compositesb.2016.06.058
46. Tomec, D. K.; K. M. Use of Wood in Additive Manufacturing: Review and Future Prospects. *Polymers* 2022, 14(6), 1174. https://doi.org/10.3390/polym14061174
47. Yip, W. C.; Yusuf, Y.; Mastura, M. T. Life Cycle Analysis (LCA) Using CES-Edupack Software of New Wood Dust Reinforced Recycled Polypropylene Composite Filament for Fused Deposition Modelling (FDM). *Lecture Notes in Mechanical Engineering* 2022, 236–240. https://doi.org/10.1007/978-981-19-3179-6_42